High-performance broadband photodetector based on $PtSe_2/MoS_2$ heterojunction from visible to near-infrared region

Bin WANG[1,3†], Jian YUAN[2,4†], Mengqi CHE[1,3], Mingxiu LIU[1,3], Yuting ZOU[1,3], Junru AN[1,3], Fan TAN[1,3], Yaru SHI[1,3], Nan ZHANG[1,3], Liujian QI[1,3], & Shaojuan LI[1,3]*.

[1] State Key Laboratory of Luminescence and Applications, Changchun Institute of Optics, Fine Mechanics and Physics, Chinese Academy of Sciences, Changchun 130033, China
[2] State Key Laboratory of Applied Optics, Changchun Institute of Optics, Fine Mechanics and Physics, Chinese Academy of Sciences, Changchun 130033, China
[3] University of Chinese Academy of Sciences, Beijing 100049, China
[4] School of Physics and Electronic Information, Huaibei Normal University, Huaibei 235000, China

* Corresponding author (email: lishaojuan@ciomp.ac.cn)
† Wang B and Yuan J have the same contribution to this work.

Supporting Information

Experimental Section:

1. Fabrication of the $PtSe_2/MoS_2$ Heterojunction Photodetectors.

The $PtSe_2$ film was produced by using the chemical vapor deposition (CVD) approach in a double heating area furnace [1]. The schematic diagram of $PtSe_2$ CVD growth is shown in Figure S1. The Si/SiO_2 wafer was selected as the substrate. First, the arrays of periodic square holes were formed on photoresist by a typical photolithography process. Subsequently, 3 nm Pt was evaporated into the corresponding square holes by means of electron beam evaporation. Then, the Pt metal periodic squares were formed on the substrate through a lift-off technique. After this, the Pt-coated SiO_2/Si substrate was placed into the quartz tube at the downstream and heated to 450 °C. Selenium powder was put at the upstream with 230 °C and was then carried to the SiO_2/Si substrate by argon (Ar, flow rate: 50 sccm) so as to react with Pt. The SiO_2/Si substrate with Pt was maintained at 450 °C for 2 h and Pt was converted to $PtSe_2$ during this process. The MoS_2 was achieved from the single crystal using mechanical exfoliation method. The $PtSe_2/MoS_2$ heterojunctions were fabricated with the transfer method, which transferring the MoS_2 to the CVD produced $PtSe_2$ film. The UV lithography was used to fabricate the source-drain electrode pattern onto the $PtSe_2/MoS_2$ heterojunctions and then Ti and Au with thicknesses of 10 and 80 nm were subsequently evaporated to form the source-drain electrodes.

2. Characterization of $PtSe_2/MoS_2$ Heterojunction Devices.

The morphology of the synthesized materials was investigated by optical microscopy (Olympus). The thicknesses of the materials were characterized by atomic force microscopy (AFM, Cypher S). X-ray photoelectron spectroscopy (XPS, Kratos

Analytical C.O.) study was carried out to measure the elemental binding energies. The XPS instrument kept the base pressure at 1×10^{-10} mbar when used to acquire core-level XPS spectra from the sample. The spectrometer used Al Kα excitation source (hν = 1486.6 eV), and the electron emission angle was 55° The size of the analyzed area was a circle of 650 μm in diameter. And the charge neutralizer was used. The energy dispersive X-ray spectroscopy (EDS) analysis was carried out by scanning electron microscopy (SEM, Phenom ProX). The micro-Raman spectroscopy (Wetic) at a 532 nm illumination laser was used to characterize the Raman and PL properties. The properties of photoresponse, response speed, imaging detection of the heterostructure were measured using a home-built test system (METATEST, E2) equipped with a semiconductor device analyzer (Keithley 4200).

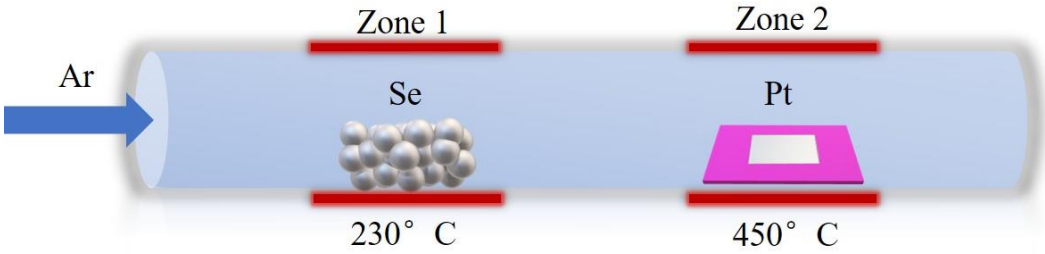

Figure S1. The schematic diagram of $PtSe_2$ CVD growth.

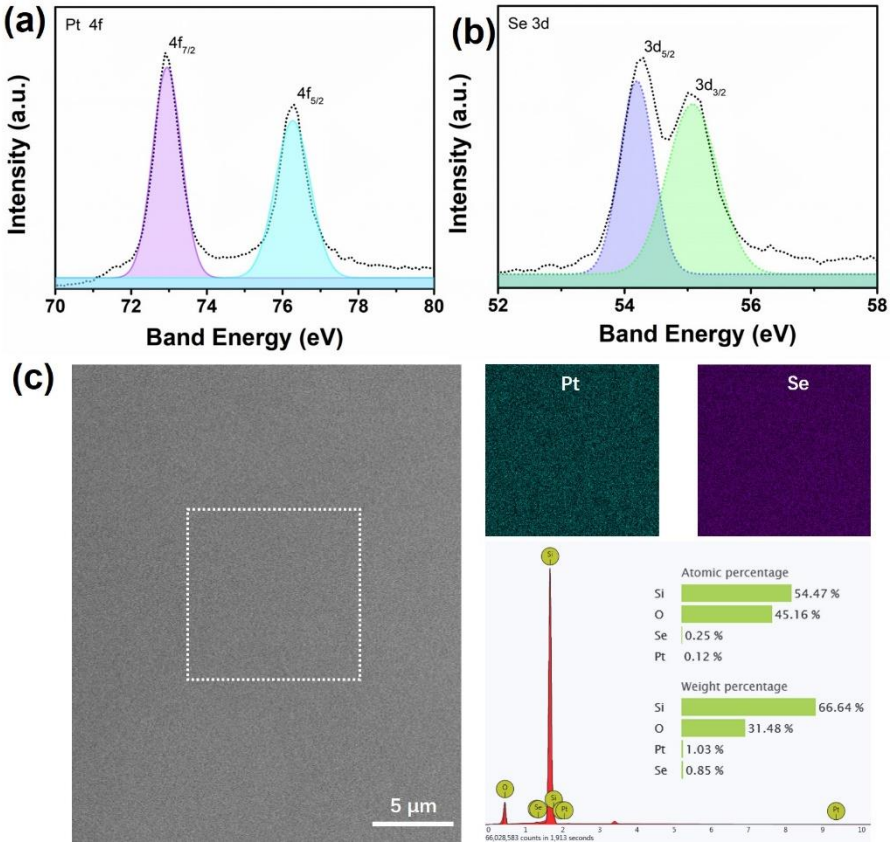

Figure S2. (a), (b) The XPS curves of $PtSe_2$ film. (c) The EDS images of $PtSe_2$ film.

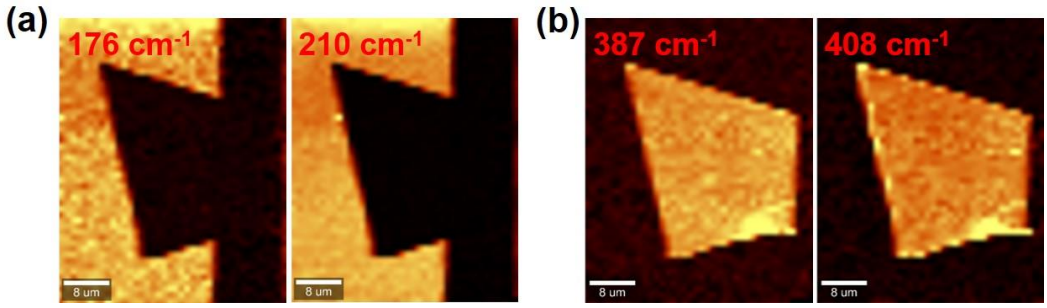

Figure S3. The Raman mapping images of $PtSe_2$ film.

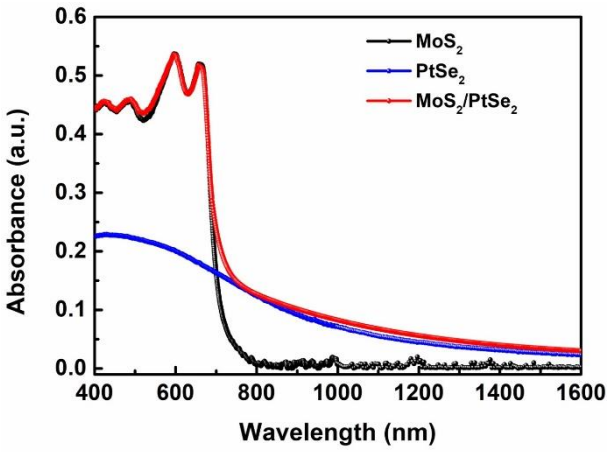

Figure S4. The absorption spectrum of the MoS_2, $PtSe_2$, and $PtSe_2/MoS_2$ heterojunction.

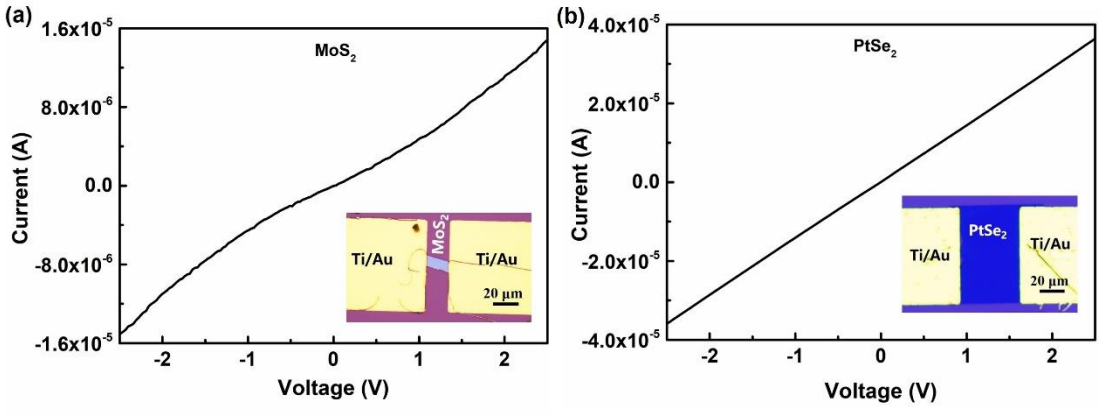

Figure S5. The I-V curves of individual MoS_2 and $PtSe_2$ devices under dark, inset is the optical images of MoS_2 and $PtSe_2$ devices.

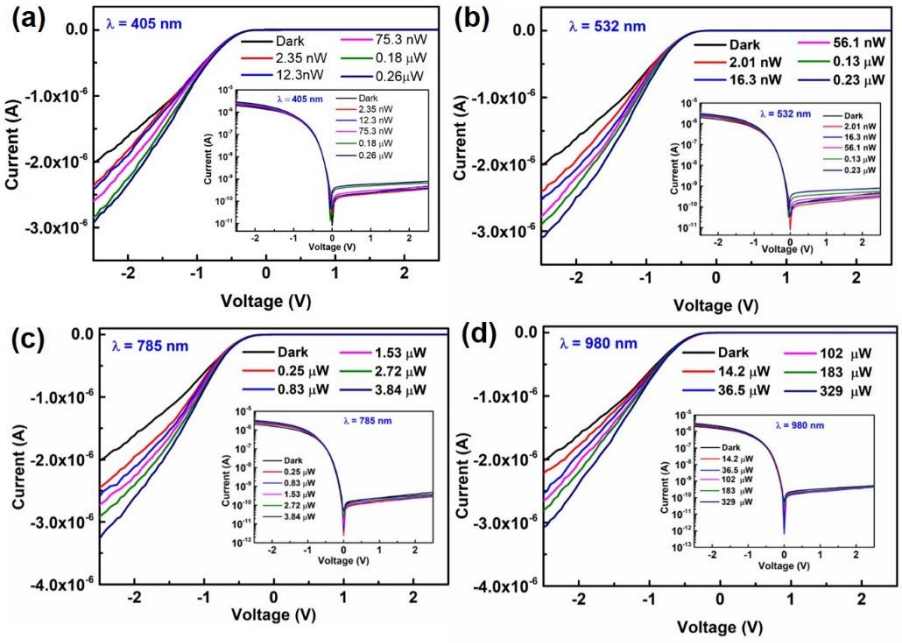

Figure S6. The I-V curves of $PtSe_2/MoS_2$ device under laser illumination (405, 532, 785, and 980 nm) with various intensities.

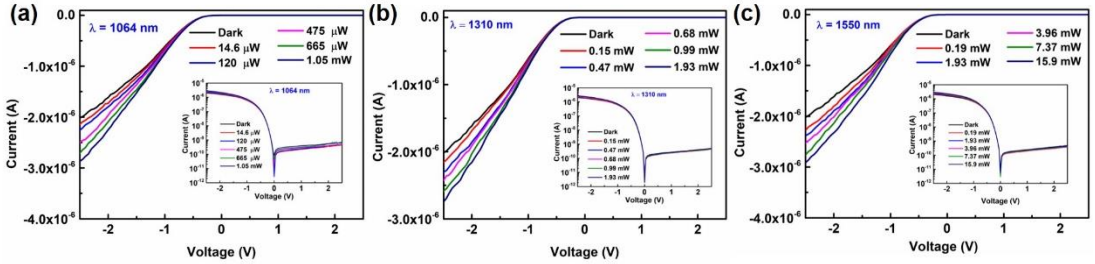

Figure S7. The I-V curves of $PtSe_2/MoS_2$ device under laser illumination (1064, 1310, and 1550 nm) with various intensities.

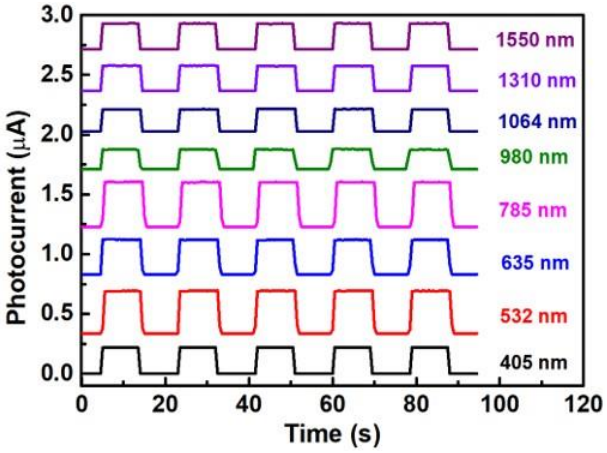

Figure S8. The time-dependent photocurrent response under laser illumination with different wavelengths (405, 532, 635, 785, 980, 1064, 1310, and 1550 nm, V_{ds} = -2 V).

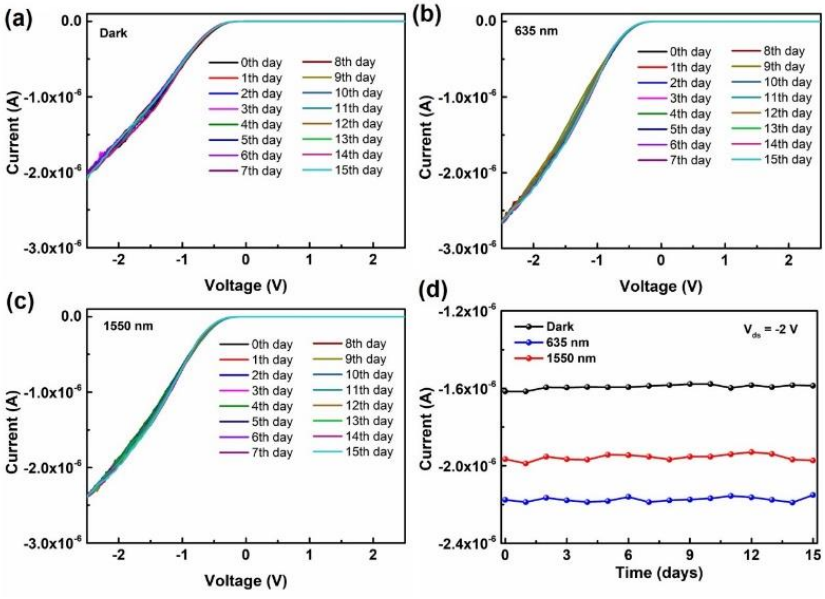

Figure S9. The stabilities of $PtSe_2/MoS_2$ device under dark and light (635 and 1550 nm) during 15 days (in air at room temperature).

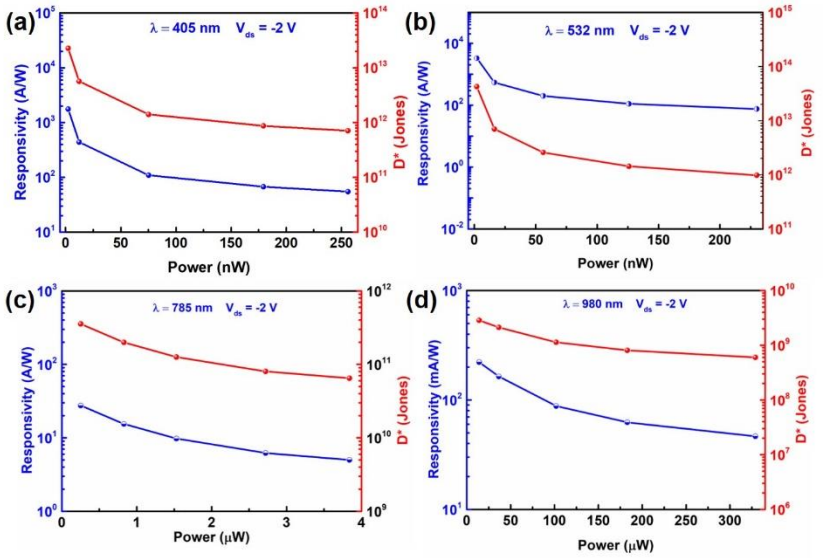

Figure S10. The responsivity and D* of $PtSe_2/MoS_2$ device as a function of laser illumination intensity (405, 532, 785, and 980 nm, V_{ds} = -2 V).

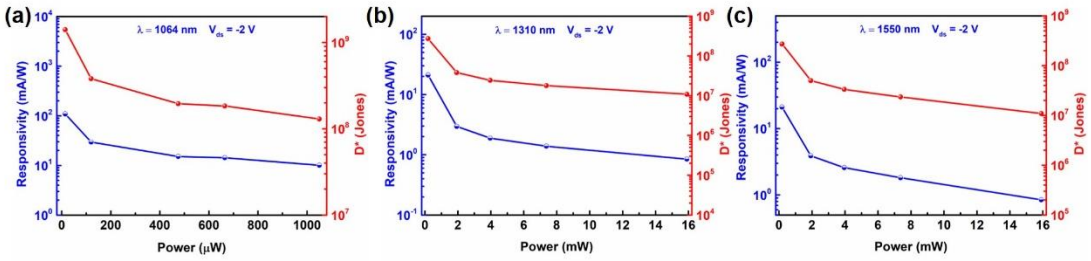

Figure S11. The responsivity and D* of $PtSe_2/MoS_2$ device as a function of laser illumination intensity (1064, 1310, and 1550 nm, V_{ds} = -2 V).

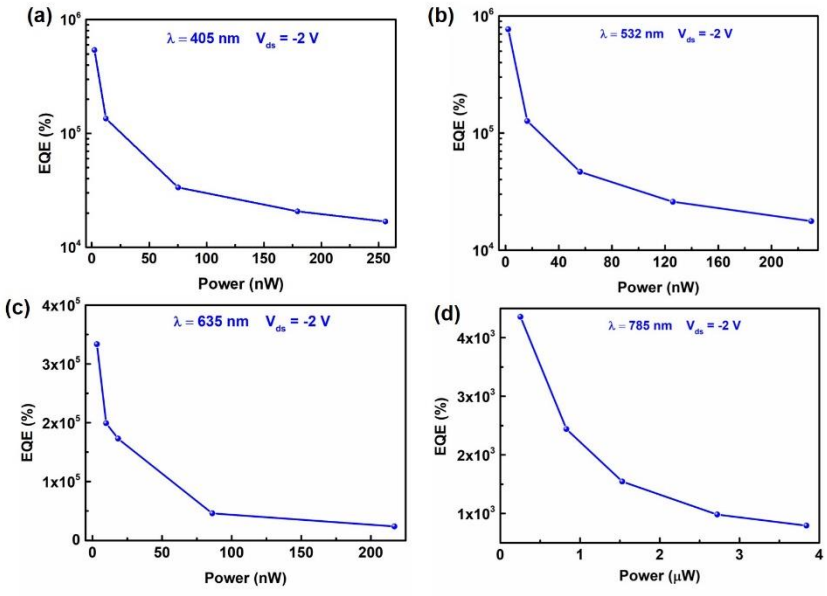

Figure S12. The EQE of $PtSe_2/MoS_2$ device as a function of laser illumination intensity (405, 532, 635, , and 785, V_{ds} = -2 V).

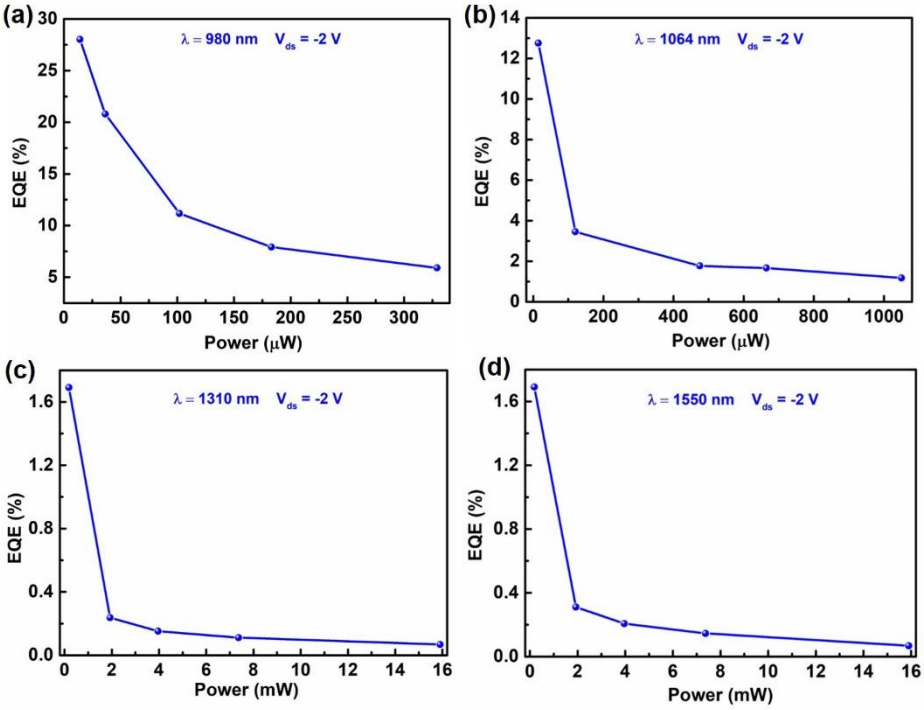

Figure S13. The EQE of $PtSe_2/MoS_2$ device as a function of laser illumination intensity (980, 1064, 1310, and 1550 nm, V_{ds} = -2 V).

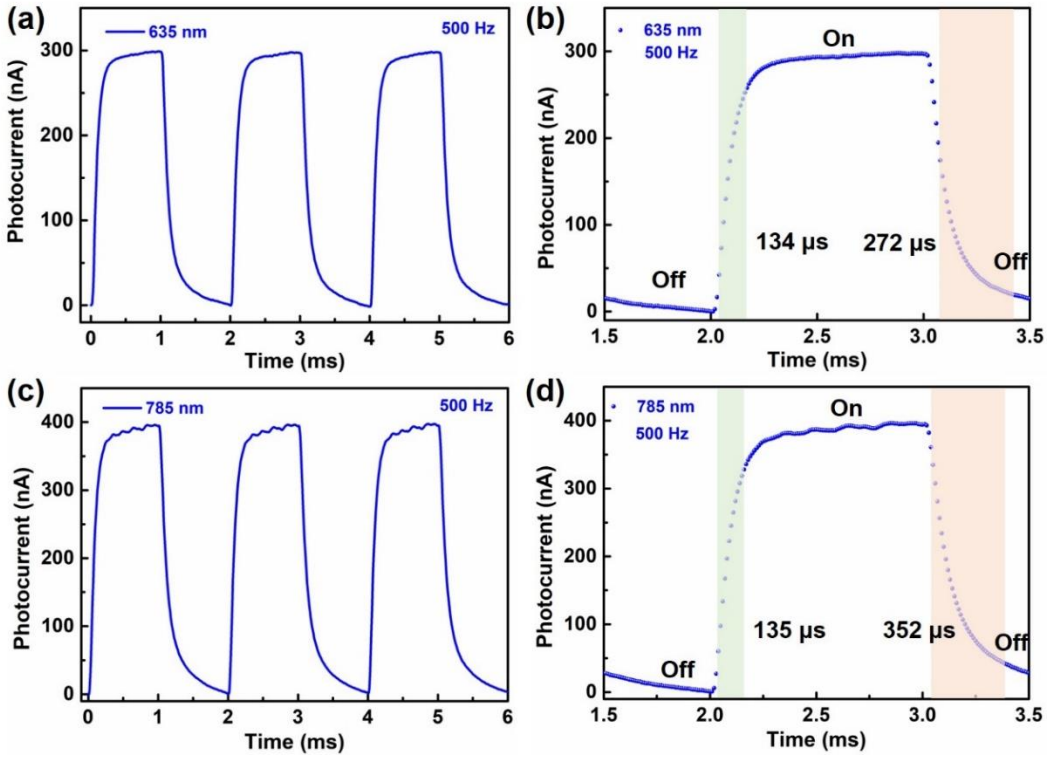

Figure S14. (a), (b) The photoresponse curve and enlarged response curve under 635 nm laser illumination at 500 Hz (V_{ds} = -2 V). (c), (d) The photoresponse curve and enlarged response curve under 785 nm laser illumination at 500 Hz (V_{ds} = -2 V).

Table S1. Comparison of $PtSe_2/MoS_2$ heterostructure photodetector with recently developed other $PtSe_2$ based photodetector.

Device Structure	Spectral Range (nm)	λ (nm)	Rectification Ratio	R (A/W)	D* (Jones)	τ_r/τ_f	Refs
$PtSe_2/MoS_2$	532-1550	635	10^4	1.7×10^3	2.2×10^{13}	134/272 μs	**This work**
$PtSe_2/MoS_2$	532-1550	785	10^4	27.52	3.55×10^{11}	135/352 μs	**This work**
$PtSe_2/MoS_2$	532-1550	1550	10^4	0.021	2.72×10^8	131/241 μs	**This work**
$PtS_2/PtSe_2$	405-2200	1064	10^1	0.050	—	66/75 ms	[1]
$PtSe_2$/GaAs	200-1200	808	10^2	0.262	2.25×10^{12}	5.5/6.5 μs	[2]

$PtSe_2$/Si	200-1550	808 1550	10^4	0.520 5.7×10^{-4}	3.26×10^{13} —	55.3/170.5 μs —	[3]
$PtSe_2$/GaN	UV	265	10^4	0.193	3.810^{14}	45/102μs	[4]
Graphene/ $PtSe_2$/β-$Ga2O_3$	225-400	245	10^4	0.076	1.93×10^{13}	12/212 μs	[5]
$PtSe_2$/ $FA_{0.85}Cs_{0.15}PbI_3$	300-1200	808	10^1	0.118	2.91×10^{12}	78/60 ns	[6]
$PtSe_2$/CdTe	200-2000	780	10^2	0.507	4.2×10^{11}	8.1/43.6 μs	[7]
$PtSe_2$/Ge	SWIR	1550	10^2	0.766	1.1×10^{11}	54.9/56.5 μs	[8]

Reference:

1. Yuan J, Sun T, Hu Z, et al. Wafer-Scale Fabrication of Two-Dimensional PtS_2/$PtSe_2$ Heterojunctions for Efficient and Broad band Photodetection. ACS Appl Mater Inter, 2018, 10: 40614-40622
2. Zeng L H, Lin S H, Li Z J, et al. Fast, Self-Driven, Air-Stable, and Broadband Photodetector Based on Vertically Aligned $PtSe_2$/GaAs Heterojunction. Adv Funct Mater, 2018, 28: 1705970
3. Xie C, Zeng L, Zhang Z, et al. High-performance broadband heterojunction photodetectors based on multilayered $PtSe_2$ directly grown on a Si substrate. Nanoscale, 2018, 10: 15285-15293
4. Zhuo R, Zeng L, Yuan H, et al. In-situ fabrication of $PtSe_2$/GaN heterojunction for self-powered deep ultraviolet photodetector with ultrahigh current on/off ratio and detectivity. Nano Res, 2018, 12: 183-189
5. Wu D, Zhao Z, Lu W, et al. Highly sensitive solar-blind deep ultraviolet photodetector based on graphene/$PtSe_2$/β-Ga_2O_3 2D/3D Schottky junction with ultrafast speed. Nano Res, 2021, 14: 1973-1979
6. Zhang Z X, Zeng L H, Tong X W, et al. Ultrafast, Self-Driven, and Air-Stable Photodetectors Based on Multilayer $PtSe_2$/Perovskite Heterojunctions. J Phys Chem Lett, 2018, 9: 1185-1194
7. Wu D, Wang Y, Zeng L, et al. Design of 2D Layered $PtSe_2$ Heterojunction for the High-Performance, Room-Temperature, Broadband, Infrared Photodetector. ACS Photonics, 2018, 5: 3820-3827
8. Lu Y, Wang Y, Xu C, et al. Construction of $PtSe_2$/Ge heterostructure-based short-wavelength infrared photodetector array for image sensing and optical communication applications. Nanoscale, 2021, 13: 7606-7612